

# Dual attitude and parameter estimation of passively magnetically stabilized nano satellites<sup>☆</sup>



R. Burton<sup>a,\*</sup>, S. Rock<sup>a</sup>, J. Springmann<sup>b</sup>, J. Cutler<sup>b</sup>

<sup>a</sup> Stanford University, 496 Lomita Mall, Stanford, CA 94305, United States

<sup>b</sup> University of Michigan, 1320 Beal Ave, Ann Arbor, MI 48109, United States

## ARTICLE INFO

### Article history:

Received 28 February 2013

Received in revised form

23 June 2013

Accepted 23 August 2013

Available online 2 September 2013

### Keywords:

Attitude determination

Nano satellites

Passive magnetic stabilization

Batch estimation

Non convex optimization

Cubesat

## ABSTRACT

The attitude determination capability of a nano satellite is limited by a lack of traditional high performance attitude sensors, a result of having small budgets for mass and power. Attitude determination can still be performed on a nano satellite with low fidelity sensors, but an accurate model of the spacecraft attitude dynamics is required. The passive magnetic stabilization systems commonly employed in nano satellites are known to introduce uncertainties in the parameters of the attitude dynamics model that cannot easily be resolved prior to launch. In this paper, a batch estimation problem is formulated that simultaneously solves for the attitude of the spacecraft and performs parameter estimation on the magnetic properties of the magnetic materials using only a measurement of the solar vector. The estimation technique is applied to data from NASA Ames Research Center's O/OREOS nano satellite and the University of Michigan's RAX-1 nano satellite, where clear differences are detected between the magnetic properties as measured before launch and those that fit the observed data. To date this is the first known on-orbit verification of the attitude dynamics model of a passively magnetically stabilized spacecraft.

© 2013 Published by Elsevier Ltd. on behalf of IAA.

## 1. Introduction

On large spacecraft, high precision attitude determination can be performed using high performance sensors such as star trackers and inertial grade gyros. On nano satellites, such as RAX-1 illustrated in Fig. 1, such instrumentation is not available due to small budgets for mass, volume and power. Furthermore, any attitude sensor that is used will take away valuable budget from the science payload. Consequently it is desirable to be able to perform attitude determination on a nano satellite using few, small sensors.

A candidate minimal sensor set would be the spacecraft's own solar panels. By using the existing solar panels, no additional components are being added to the spacecraft, and no additional mass, volume or power budget is being used. From differential solar panel currents, an estimate of the

solar vector can be obtained, and this can be used to perform attitude determination.

Attitude determination can still be performed on a nano satellite using only a measurement of the solar vector, but an estimator that incorporates an accurate spacecraft attitude dynamics model is required.

The same low mass and power budgets that negate the use of high performance attitude sensors also encourage the use of passive magnetic stabilization systems in nano satellites. These passive magnetic systems require no power and have low mass and volume requirements. Passive magnetic systems typically consist of a permanent dipole that provides alignment to the Earth's magnetic field, and magnetically permeable material that provides damping for the removal of excess rotational kinetic energy. An accurate attitude dynamics model for a passively magnetically stabilized spacecraft requires an accurate model of the torques generated from the interaction of these magnetic components with the Earth's magnetic field.

While the torque arising from a permanent dipole of known strength in an external magnetic field is trivially

<sup>☆</sup> This paper was presented during the 63rd IAC in Naples.

\* Corresponding author. Tel.: +1 646 449 7588.

E-mail address: [rolandb@stanford.edu](mailto:rolandb@stanford.edu) (R. Burton).

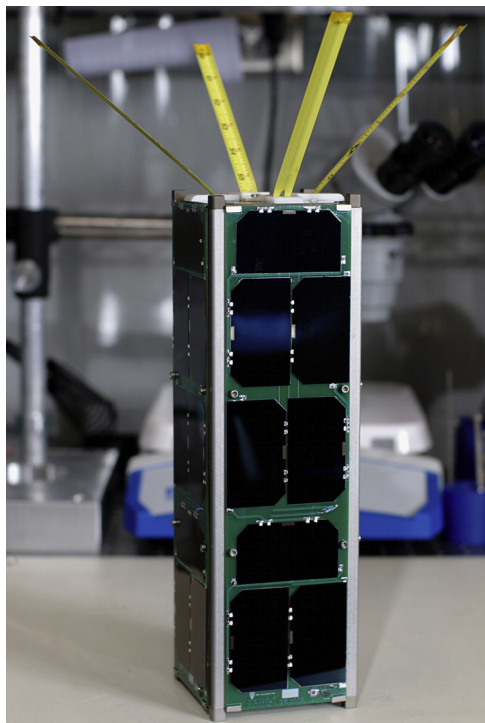


Fig. 1. University of Michigan RAX-1 3U CubeSat.

computed, the magnetically permeable material poses more of a challenge due to non-linear time-variant dynamics, and the presence of additional states that are not directly observable. These dynamics have been studied well for isolated samples of material in a laboratory [1], and in such situations the material's properties can be accurately characterized. To date there has been no demonstration of the fidelity of these models when included in a full attitude dynamics simulation.

When the magnetic components are installed in a spacecraft the magnetic properties will change due to interactions both with similar material installed in close proximity, and also to other spacecraft components. Pre-launch testing in the laboratory of a complete system is hampered by the very small torques produced, and the difficulty in maintaining a magnetically clean environment. The differences between laboratory measured properties and the effective installed properties have been substantially enough to cause problems with attitude determination, with previous nano satellite missions observing disagreements between pre-launch simulations and observed attitude profiles [2]. In many cases, the observed bus measurements cannot be reproduced using the pre-launch dynamics model, as demonstrated in Fig. 2, which compares bus solar data to that derived from simulation.

An alternative approach to characterizing the magnetic properties in order to obtain an accurate attitude dynamics model is to calibrate the magnetic properties using on-orbit data. Specifically parameter estimation can be performed to fit a dynamics model to the observed data. As the on-orbit measurements are attitude dependent, the attitude determination and parameter estimation problems need to be solved simultaneously.

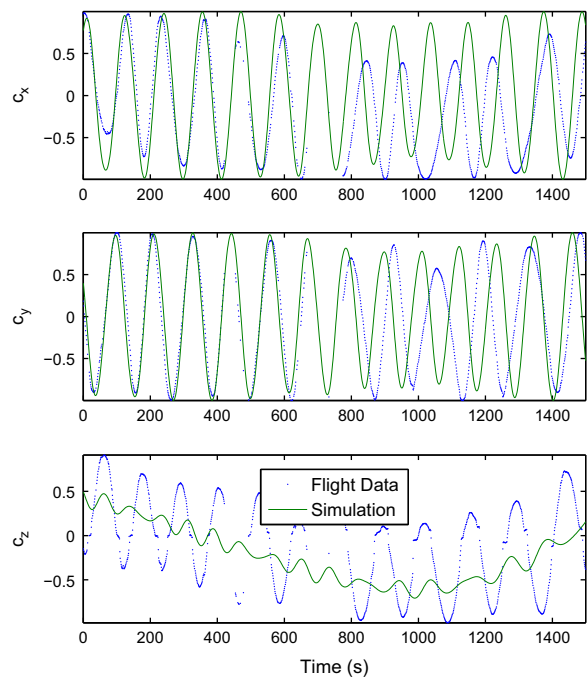


Fig. 2. Comparison of solar vector components for RAX-1. 30-Dec-2010 14:28:15 UTC. Pre-launch estimated dipole used. Note large errors between observed data and simulation.

In Section 2 of this paper, a batch estimation framework is developed to calibrate the parameters of the dynamics model of a passively magnetically stabilized nano satellite. The batch estimation technique is applied to actual flight data from two different nano satellites, and the results are presented in Section 3. Clear differences are detected between the magnetic properties as measured before launch and those found through calibration, and an attitude estimation accuracy of better than  $5^\circ$  is demonstrated.

## 2. Method

The estimation problem can be described as finding a set of initial conditions and parameters that reproduce in simulation the measured data as closely as possible. This can be formulated as a non-convex optimization problem, Eq. (1), where initial conditions,  $x_0$ , and system parameters,  $\theta$ , are iterated upon until simulated data matches measured data:

$$\begin{aligned} & \underset{x_0, \theta}{\text{minimize}} && \sum_{k=1}^m \|\tilde{y}_k - h(\hat{x}(t_k), t_k)\|_2^2 \\ & \text{subject to :} && \dot{\hat{x}}(t) = f(\hat{x}(t), \theta, t) \\ & && \hat{x}(t_0) = x_0 \end{aligned} \quad (1)$$

In the application studied in this paper, the function  $f(x(t), \theta, t)$  in Eq. (1) describes the attitude dynamics of a passively magnetically stabilized spacecraft. The state  $x(t)$  includes both the kinematic attitude state and an additional state required to model the time variant behavior of the magnetic permeable material. The parameters of the dynamical system,  $\theta$ , are any constants in the state dynamics that

are unknown or require calibration, and in this work are the properties of the magnetic materials in the system and the inertia matrix,  $I$ . The attitude dynamics are described in detail in Section 2.1.

The measurements,  $\hat{y}_k$ , are an estimate of the solar vector, obtained from solar panel currents of photodiode voltages. The measurement function  $h(x, t)$  simulates the measurements, and both are described in Section 2.3.

### 2.1. Attitude dynamics

$$\dot{q} = \frac{1}{2}\omega \otimes q \quad (2)$$

$$T = I\dot{\omega} + \omega \times I\omega \quad (3)$$

The attitude kinematics and dynamics for a rigid body are given by Eqs. (2) and (3) respectively. In Eq. (2) the unit quaternion is used to represent the spacecraft's attitude and  $\omega$  is the body angular rate in the body frame. The symbol  $\otimes$  denotes quaternion multiplication as defined in Ref. [3].

In Eq. (3) the external torque  $T$  includes parasitic environmental torques in addition to any control torques. In the case of a passively magnetically stabilized spacecraft these control torques will arise from the interaction of the installed magnetic dipoles with the Earth's magnetic field. Typical expected values of the environmental torques were estimated for a 3U (0.3 m × 0.1 m × 0.1 m) CubeSat in a 650 km low Earth orbit and are listed in Table 1, along with nominal values for the torques from a typical passive magnetic stabilization system. As the parasitic torques are several orders of magnitude lower than those from the magnetics, it is reasonable to ignore them in the attitude dynamics model, and only include the magnetic torque in Eq. (3).

**Table 1**  
Torques acting on the spacecraft.

Torque source	Nominal value (N m)
Magnetic dipole	$5 \times 10^{-5}$
Gravity gradient	$3 \times 10^{-8}$
Solar radiation pressure	$2 \times 10^{-8}$
Aerodynamic pressure	$2 \times 10^{-9}$

#### 2.1.1. Magnetic torques

In a typical passive magnetic system, permanent dipoles are aligned with the desired spin axis, and magnetically permeable rods are mounted in the plane perpendicular to the axis. The permanent dipoles provide alignment to the Earth's magnetic field, and the magnetically permeable material provides damping of excessive angular motions post separation. Fig. 3(a) shows an estimate of the rotational kinetic energy time history of a nano satellite over 30 days following separation from the launch vehicle. During the first 15 days, when the spacecraft is still finishing de-tumbling, the permeable rods provide the dominant source of damping. After 15 days, the permeable rods become latched, no longer provide a significant source of damping, and the spacecraft enters a steady state. The science mission is typically carried out during this phase. Fig. 3(b) illustrates a typical installed configuration, where four vertical (z aligned) permanent dipoles and two horizontal (x and y aligned) permeable rods are employed.

The torque from a dipole of strength  $M$  in a magnetic field  $H$  is given by Eq. (4) where  $\mu_0$  is the permeability of free space. In a system consisting of both permanent dipoles and magnetically permeable material the torque can be computed using Eq. (5) where  $M_p$  is the strength of the permanent dipole, and  $B_i(t)$  is the time varying induced flux density in the  $i$ th permeable rod of volume  $V_i$ . The rod is aligned along unit vector  $n_i$ :

$$T = \mu_0(M \times H) \quad (4)$$

$$T = \left( \sum_{i=1}^N n_i B_i(t) V_i + \mu_0 M_p \right) \times H \quad (5)$$

The external magnetic field,  $H$ , in the body frame is a function of orbital position, which is assumed known, and the spacecraft attitude. The effective installed permanent dipole,  $M_p$ , and the effective permeable rod volume,  $V$ , are both assumed to be unknown constant parameters. The induced magnetic flux density in the rod,  $B$ , is time variant, so the state dynamics  $f(x(t), \theta, t)$  must include the dynamics of the permeable material to allow the torque to be computed.

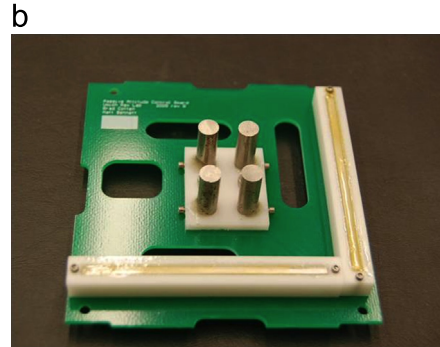
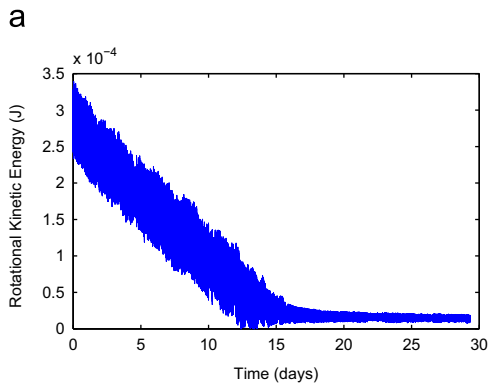


**Fig. 3.** Passive magnetic stabilization systems. (a) Estimate of rotational kinetic energy history of RAX-1 nano satellite after separation from launch vehicle. (b) Magnetic components of RAX-1 nano satellite.

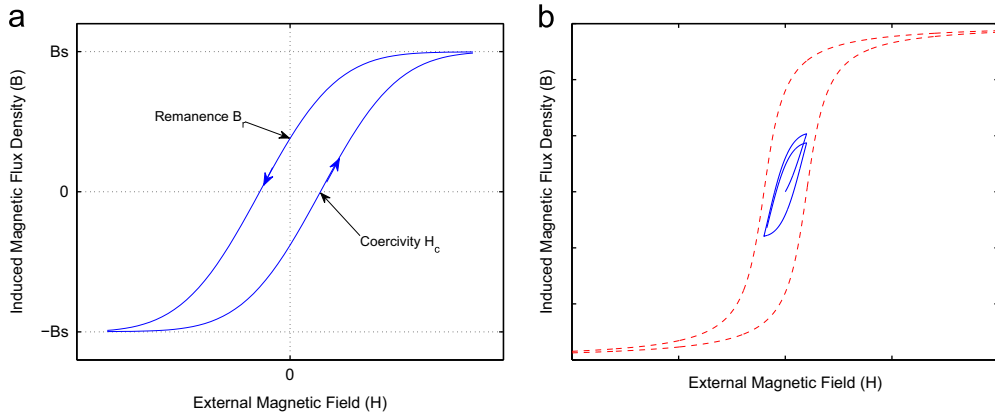


Fig. 4. Modeling magnetically permeable material. (a) Typical hysteresis loop. (b) Simulation of hysteresis loop.

In Eq. (5) it is assumed that linear superposition of multiple permanent dipoles can be used, and so all permanent dipoles can be combined as one permanent dipole.

### 2.1.2. Hysteresis modeling

If a permeable rod is placed in a time varying magnetic field with component  $H$  along the long axis of the rod, the flux density induced in the rod,  $B$ , lags changes in the external field, a phenomenon known as hysteresis. The three magnetic properties of permeable material that describe the shape of these hysteresis loops, as illustrated in Fig. 4(a), are the saturation flux density  $B_s$ ; the remanence flux density  $B_r$ ; and the coercivity  $H_c$ .

Fatley and Henretty [1] proposed an empirical model to describe both the bounding curves of the hysteresis material and the behavior in the region between the two curves. The bounding curves are described by the inverse tangent function equation (6). Eq. (7) is the empirically derived differential equation that describes the behavior at any point  $(H, B)$  between the limits. The derived material property  $k$  is called the shape parameter. A sample simulated hysteresis loop is illustrated in Fig. 4(b) where the external field was varied between  $\pm H_c$ :

$$B_{lim}(H) = B_s \left( \frac{2}{\pi} \right) \text{atan}(k(H \pm H_c)) \quad (6)$$

$$\frac{dB}{dH} = \frac{2}{\pi} k B_s \cos^2 \left( \frac{\pi B}{2B_s} \right) \left( \frac{H - H_{lim}(B)}{2H_c} \right)^2 \quad (7)$$

where

$$k = \frac{1}{H_c} \tan \left( \frac{\pi B_r}{2B_s} \right) \quad (8)$$

$$H_{lim}(B) = \frac{1}{k} \tan \left( \frac{\pi B}{2B_s} \right) \pm H_c \quad (9)$$

If both the component of the external field aligned with the rod,  $H$ , and the time rate of change of this component,  $\dot{H}$ , are known then magnetically permeable material can be included in a dynamical system by augmenting the existing states with the induced flux density,  $B$ , and augmenting the

state update equations with

$$\frac{dB}{dt} = \frac{dB}{dH} \frac{dH}{dt} \quad (10)$$

It has been shown [4] that significant computational advantages are obtained by integrating a substituted modified flux state,  $S$ , as defined in Eq. (11) rather than directly integrating the induced flux density,  $B$ :

$$S = \tan \left( \frac{\pi B}{2B_s} \right) \quad (11)$$

The bounding limits and differential equation describing the behavior between the limits are described in Eqs. (12) and (13) respectively. Integrating the modified flux density,  $S$ , rather than the induced flux density,  $B$ , involves fewer transcendental function evaluations and operations close to  $(\tan \frac{\pi}{2})$ :

$$S_{lim} = k(H \pm H_c) \quad (12)$$

$$\frac{dS}{dH} = k \left( \frac{H - \frac{S}{k} \pm H_c}{2H_c} \right)^2 \quad (13)$$

$$\frac{dS}{dt} = \frac{dS}{dH} \frac{dH}{dt} \quad (14)$$

The substitution offers faster numerical convergence, allowing a larger integration time step and an order of magnitude improvement in integration speed. This speed increase becomes of great value in the optimization performed in this paper, where multiple evaluations are required per step to compute finite difference gradients.

A separate modified flux state,  $S_i$ , must be propagated for each of the  $N$  installed rods.

### 2.1.3. External magnetic field

Computation of the torque also requires knowledge of the external magnetic field in the body frame. Computing the time derivative of the induced magnetic flux density in the rod, Eqs. (10) and (14), additionally requires knowledge of the time rate of change of the external field.

Assuming that the spacecraft's orbital position is known, then the external magnetic field in an inertial frame,  $H_{ECI}$ , can be computed from the IGRF [5] model. If it is assumed that

the orbital position is independent of the spacecraft's attitude then the spacecraft's orbital position can be propagated independently and the inertial time derivative of the magnetic field in the inertial frame,  $\dot{H}_{\text{ECI}}$ , computed. From these, the external magnetic field,  $H$ , and its body frame time derivative,  $\dot{H}$ , in the body frame can then be calculated using Eqs. (15) and (16) respectively:

$$H = q \otimes H_{\text{ECI}} \otimes q^{-1} \quad (15)$$

$$\dot{H} = q \otimes \dot{H}_{\text{ECI}} \otimes q^{-1} - \omega \times H \quad (16)$$

#### 2.1.4. Summary of attitude dynamics

The system state  $x$  consists of the attitude, attitude rates, and the modified flux state of each of the  $N$  permeable rods, as in the following equation:

$$x(t) = \begin{bmatrix} q(t) \\ \omega(t) \\ S_1(t) \\ \vdots \\ S_N(t) \end{bmatrix} \quad (17)$$

The full attitude dynamics of a passively magnetically stabilized spacecraft are summarized in the following equations:

$$\dot{q}(t) = \frac{1}{2} \omega(t) \otimes q(t) \quad (18)$$

$$\dot{\omega}(t) = I^{-1} \left[ \left( \sum_{i=1}^N \frac{2}{\pi} e_i B_{s_i} V_i \operatorname{atan}(S_i(t)) + \mu_0 M_P \right) \times H(t) - \omega(t) \times I \omega(t) \right] \quad (19)$$

$$\dot{S}_i(t) = k_i n_i^T \dot{H}(t) \left( \frac{n_i^T H(t) - \frac{1}{k} S_i(t) \pm H_{c_i}}{2 H_{c_i}} \right)^2, \quad i = 1 \dots N \quad (20)$$

where

$$H(t) = q(t) \otimes H_{\text{ECI}}(t) \otimes q^{-1}(t) \quad (21)$$

$$\dot{H}(t) = q(t) \otimes \dot{H}_{\text{ECI}}(t) \otimes q^{-1}(t) - \omega(t) \times H(t) \quad (22)$$

## 2.2. Parameters

In this paper, the batch dynamics estimation method is applied during the science phase of the mission, where an attitude determination capability is most useful. In the science phase, when the spacecraft is in a steady state, the magnetically permeable rods are assumed to no longer be providing a significant source of damping and the magnetic torque is dominated by the permeant dipole.

The parameters being optimized over,  $\theta$ , are the moments of inertia and the permanent dipole, as defined in Eq. (23), where  $\bar{I}$  denotes a vector of the six unique parameters in the inertia matrix  $I$ :

$$\theta = \begin{bmatrix} \bar{I} \\ M_P \end{bmatrix} \quad (23)$$

The magnetically permeable material is still included in the dynamics model, and the required properties,  $B_r$ ,  $B_s$  and  $H_c$ , are obtained by performing a separate batch estimation using data that captures the damping effect of the permeable material [6]. For example, in the case of the RAX-1 nano satellite, data was used that covered a period of 30 days, starting 10 days after launch.

## 2.3. Measurement function

In this work, it is assumed that the only measurement available to the spacecraft is an estimate of the solar vector in the body frame. This can be obtained from solar panel currents, or from photodiode voltages if they are available. Fig. 5 describes the general process for obtaining an estimate of the solar vector from raw readings. It is assumed that the normals of the faces of the spacecraft are aligned with the  $\pm x$ ,  $\pm y$  and  $\pm z$  body axes.

The raw readings are first shifted so that the minimum reading is zero, which takes account of bias in the measurement. Following this the shifted raw readings are scaled so that the maximum value is one, using a backwards looking window. This scaling is designed to take into account sensor degradation over time. Next, the readings from the negative facing panels are subtracted from the positive facing readings to obtain a unit vector component in  $x$ ,  $y$  and  $z$ . Finally these components are combined and scaled to unit length. It is not expected that

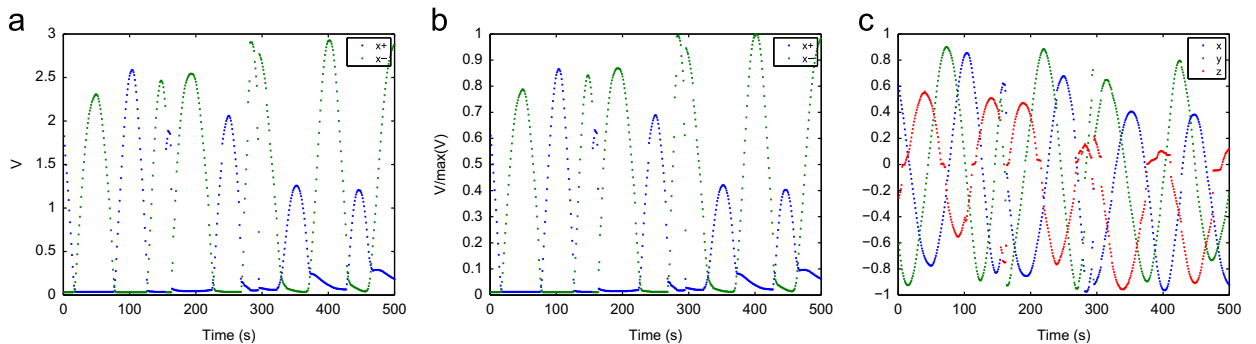


Fig. 5. Estimating the solar vector. (a) Raw sensor readings ( $\pm x$  only). (b) Scaled sensor readings ( $\pm x$  only). (c) Final estimate ( $x, y, z$  components).



this final scaling will change the components significantly, and for the data from RAX-1, the unscaled length was in the range 0.97–1.02.

The solar vector in the body frame,  $c$ , is related to the solar vector in the inertial frame,  $c_{\text{ECI}}$ , via the following equation:

$$c = q \otimes c_{\text{ECI}} \otimes q^{-1} \quad (24)$$

The solar vector in the inertial frame is assumed known, and is a function of the spacecraft's orbital position. Eq. (24) is the measurement function,  $h(x(t), t)$ , as required in the optimization presented in Eq. (1).

#### 2.4. Constraints

The parameters and initial conditions must be constrained to physically realizable values. If the dynamics of the system are correctly formulated, the system is stable and the initial conditions are physically realizable, then the system state will stay physically realizable and does not need to be explicitly constrained.

The constraints on the inertia matrix are given in Eq. (25). These constraints are equivalent to requiring that all the principle moments are positive, and that the sum of the smaller two principle moments is larger than the largest principle moment:

$$\begin{aligned} \text{eig}(I) &> 0 \\ \sum \text{eig}(I) &\geq 2 \max(\text{eig}(I)) \end{aligned} \quad (25)$$

The initial state  $x_0$  is constrained via the following equations:

$$\|q(t_0)\| = 1 \quad (26)$$

$$k_i(n_i^T H(t_0) - H_{c_i}) \leq S_i(t_0) \leq k_i(n_i^T H(t_0) + H_{c_i}), \quad i = 1 \dots N \quad (27)$$

#### 2.5. Simplifications

The dynamics and measurement models, as described by Eqs. (17) through (24) are non-linear and non-convex. In addition some of the constraints introduced in Section 2.4 are non-convex. To improve the tractability of the optimization, the non-convex constraints can be removed by performing some variable substitution. As an added benefit, some of these substitutions also reduce the dimension of the variables being optimized over.

1. The initial attitude  $q(t_0)$  is replaced with a three-component attitude parameterization, the Euler Angles  $(\phi_0, \theta_0, \psi_0)$ , such that  $q(t_0) = q(\phi_0, \theta_0, \psi_0)$ . This substitution reduces the dimension of state  $x_0$  size by one, and removes the non-convex equality constraint that requires  $q(t_0)$  to be of unit length.
2. The non-convex constraint described in Eq. (27) can be removed by introducing a new state,  $s_0$ , as defined in Eq. (28). The new variable,  $s_0$ , denotes the fractional position that the modified flux density,  $S_i(t_0)$ , lies between the limiting substituted flux densities  $S_{\text{lim}_i}$  evaluated at  $n_i^T H(t_0)$ , with values of  $\pm 1$  denoting the limits. The modified flux parameter initial condition

$S_i(t_0)$  can be recovered from  $s_0$  using Eq. (29).

$$s_{0_i} = \frac{S_i(t_0) - k_i n_i^T H(t_0)}{k_i H_{c_i}}, \quad i = 1 \dots N \quad (28)$$

$$S_i(t_0) = k_i(s_{0_i} H_{c_i} + n_i^T H(t_0)), \quad i = 1 \dots N \quad (29)$$

After the substitution, the non-convex constraint in Eq. (27) is replaced by the following equation, a linear constraint:

$$-1 \leq s_{0_i} \leq 1, \quad i = 1 \dots N \quad (30)$$

3. The constraints on the inertia matrix can be simplified by solving the three principle moments of inertia,  $I_1$ ,  $I_2$  and  $I_3$ , and a rotation from the principle axes to the body frame. The rotation can be parameterized by three Euler angles,  $(\phi_I, \theta_I, \psi_I)$ . Constraint equation (25), which involved computation of eigenvalues, can be replaced by linear constraints on the principle axes given in the following equations:

$$I_1 \geq I_2 \geq I_3 \quad (31)$$

$$I_2 + I_3 \geq I_1 \quad (32)$$

The full inertia matrix is linked to the principle axes via a direction cosine matrix,  $A(\phi_I, \theta_I, \psi_I)$ , parameterized by the three Euler angles,  $(\phi_I, \theta_I, \psi_I)$ , as given by the following equation:

$$I = A(\phi_I, \theta_I, \psi_I) \begin{bmatrix} I_1 & 0 & 0 \\ 0 & I_2 & 0 \\ 0 & 0 & I_3 \end{bmatrix} A(\phi_I, \theta_I, \psi_I)^T \quad (33)$$

The direction cosine matrix  $A(\phi_I, \theta_I, \psi_I)$  can be computed from the Euler angles using Eq. (45).

After the simplifications, the estimation problem as described by Eqs. (17)–(33) now has only linear inequality constraints. The cost function remains non-convex in the parameters and initial conditions.

#### 2.6. Summary of dynamics estimation problem

The optimization described in Sections 2.1–2.5 is summarized in the following equations:

$$\underset{x_0, \theta}{\text{minimize}} \quad \sum_{k=1}^N \|\tilde{c}_k - \hat{q}(t_k) \otimes c_{\text{ECI}}(t_k) \otimes \hat{q}^{-1}(t_k)\|^2 \quad (34)$$

subject to dynamics

$$\dot{\hat{q}}(t) = \frac{1}{2} \hat{\omega}(t) \otimes \hat{q}(t) \quad (35)$$

$$\begin{aligned} \dot{\hat{\omega}}(t) = I^{-1} \left[ \left( \sum_{i=1}^N \frac{2}{\pi} n_i B_{s_i} V_i \text{atan}(S_i(t)) + \mu_0 M_P \right) \right. \\ \left. \times \hat{H}(t) - \hat{\omega}(t) \times I \hat{\omega}(t) \right] \end{aligned} \quad (36)$$

$$\dot{S}_i(t) = k_i n_i^T \dot{H}(t) \left( \frac{n_i^T \hat{H}(t) - \frac{1}{k_i} S_i(t) \pm H_{c_i}}{2 H_{c_i}} \right)^2, \quad i = 1 \dots N \quad (37)$$

$$\dot{H}(t) = \hat{q}(t) \otimes H_{\text{ECI}}(t) \otimes \hat{q}^{-1}(t) \quad (38)$$

$$\dot{H}(t) = \hat{q}(t) \otimes \dot{H}_{\text{ECI}}(t) \otimes \hat{q}^{-1}(t) - \omega(t) \times \hat{H}(t) \quad (39)$$

where

$$x_0 = \begin{bmatrix} \phi_0 \\ \theta_0 \\ \psi_0 \\ \omega_0 \\ s_{0_1} \\ \vdots \\ s_{0_N} \end{bmatrix}, \quad \theta = \begin{bmatrix} I_1 \\ I_2 \\ I_3 \\ \phi_1 \\ \theta_1 \\ \psi_1 \\ M_P \end{bmatrix} \quad (40)$$

with initial state

$$\hat{q}(t_0) = q(\phi_0, \theta_0, \psi_0) \quad (41)$$

$$\hat{\omega}(t_0) = \omega_0 \quad (42)$$

$$\hat{S}_i(t_0) = k_i(s_{0_i} H_{c_i} + n_i^T \hat{H}(t_0)), \quad i = 1 \dots N \quad (43)$$

and parameters

$$I = A(\phi_1, \theta_1, \psi_1) \begin{bmatrix} I_1 & 0 & 0 \\ 0 & I_2 & 0 \\ 0 & 0 & I_3 \end{bmatrix} A(\phi_1, \theta_1, \psi_1)^T \quad (44)$$

where

$$A(\phi_1, \theta_1, \psi_1) = \begin{bmatrix} c\theta_1 c\psi_1 & c\theta_1 s\psi_1 & -s\theta_1 \\ s\phi_1 s\theta_1 c\psi_1 - c\phi_1 s\psi_1 & s\phi_1 s\theta_1 s\psi_1 + c\phi_1 c\psi_1 & s\phi_1 c\theta_1 \\ c\phi_1 s\theta_1 c\psi_1 + s\phi_1 s\psi_1 & c\phi_1 s\theta_1 s\psi_1 - s\phi_1 c\psi_1 & c\phi_1 c\theta_1 \end{bmatrix} \quad (45)$$

subject to constraints

$$-1 \leq s_{0_i} \leq 1 \quad i = 1 \dots N \quad (46)$$

$$I_1 \geq I_2 \geq I_3 \quad (47)$$

$$I_2 + I_3 \geq I_1 \quad (48)$$

## 2.7. Initial conditions for optimization

The problem summarized in Section 2.6 remains highly non-convex. Any numerical method chosen will

be suboptimal, and will at best only find a local minimum. Regardless of the numerical optimization method used to solve the problem, a good initial guess will be critical to finding a true minimum, corresponding to the best fit.

1. Initial estimates for the magnetic properties are best taken from laboratory tests. As has been shown in the previous papers [4,7], material data sheets cannot be relied upon for accurate hysteresis parameters. If no pre-launch test data is available for the samples installed, then estimates based upon tests of similar materials can be used.
2. A good estimate for the initial angular rate,  $\omega_0$ , can be found by examining the frequency content of the estimated solar vector data. A sample power spectral density for the RAX-1 spacecraft solar vector data is shown in Fig. 6 (b). In steady state it can be assumed that the spacecraft will be spinning around the permanent dipole, so an initial angular rate aligned with the permanent dipole and with the same magnitude as the peak in the power spectral density will be a reasonable initial guess.
3. An initial attitude direction cosine matrix,  $A_0$  can be estimated by solving Wahba's problem [8] at  $t_0$ . Wahba's problem determines the rotation matrix between two frames that best satisfies observations of vectors in both frames. A minimum of two independent vectors measured or known in both the body frame and inertial frame are required to produce a solution. In this problem the two vectors are the sun unit vector,  $c_{\text{ECI}}$ , and the local external magnetic field,  $H_{\text{ECI}}$ , both of which are known in the inertial frame. The measured sun vector in the body frame,  $\tilde{c}$ , is estimated from onboard sensors. An assumption can be made that the permanent dipole is aligned to the magnetic field. This will likely be a reasonable estimate once the spacecraft is operating in steady state. Following the method of Markley [9] that uses singular value decomposition to solve Wahba's problem, an initial estimate of the attitude matrix  $A_0$  is found using the following equations:

$$R = \left( \frac{M_P}{\|M_P\|} \right) \left( \frac{H_{\text{ECI}}(t_0)}{\|H_{\text{ECI}}(t_0)\|} \right)^T + \tilde{c}(t_0) c_{\text{ECI}}^T(t_0) \quad (49)$$

$$R = U \Sigma V^T \quad (50)$$

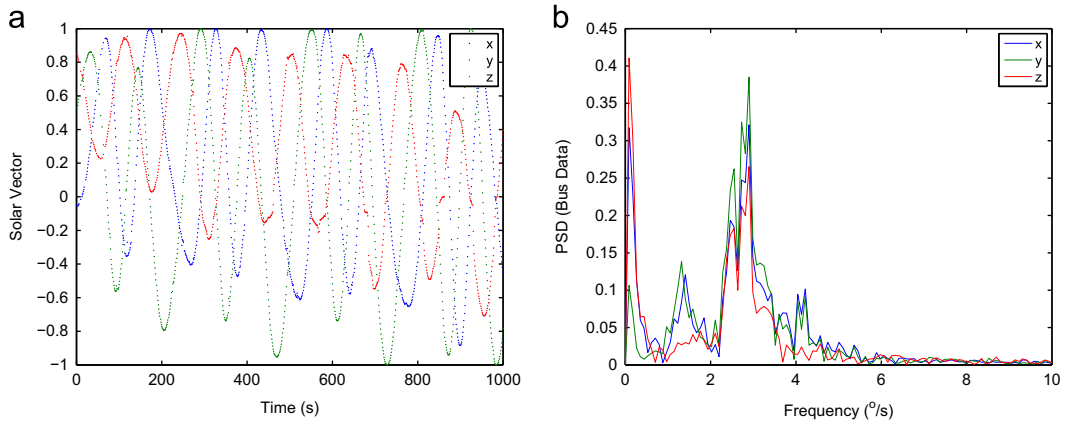


Fig. 6. Frequency analysis of solar vector bus data to get characteristic spin rate. (a) Solar vector estimate. (b) Power spectral density.

$$A_0 = U \text{diag}([1 \ 1 \ \det(U)\det(V)])V^T \quad (51)$$

The direction cosine matrix  $A$  then needs to be converted to initial Euler Angles ( $\phi_0, \theta_0, \psi_0$ ) using Eq. (52).

$$\begin{bmatrix} \phi \\ \theta \\ \psi \end{bmatrix} = \begin{bmatrix} \text{atan2}(A_{23}, A_{33}) \\ \text{asin}(A_{31}) \\ \text{atan2}(A_{12}, A_{11}) \end{bmatrix} \quad (52)$$

The result of using these three initial conditions for a simulation is shown in Fig. 7, in both the time and frequency domains. No optimization has yet been run, and pre-launch estimates for the parameters are being used. As can be seen, the fit is fairly close, but still needs some more tuning.

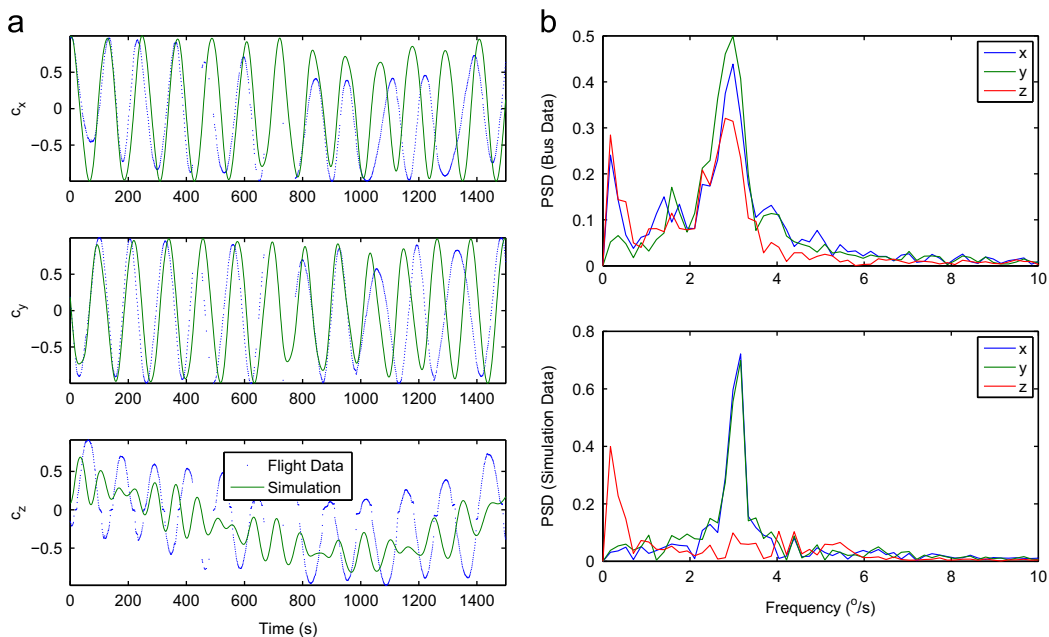


**Fig. 7.** Comparison of simulation and bus data in time and frequency domains for initial condition. (a) Solar vector fit. (b) Power spectral density comparison.

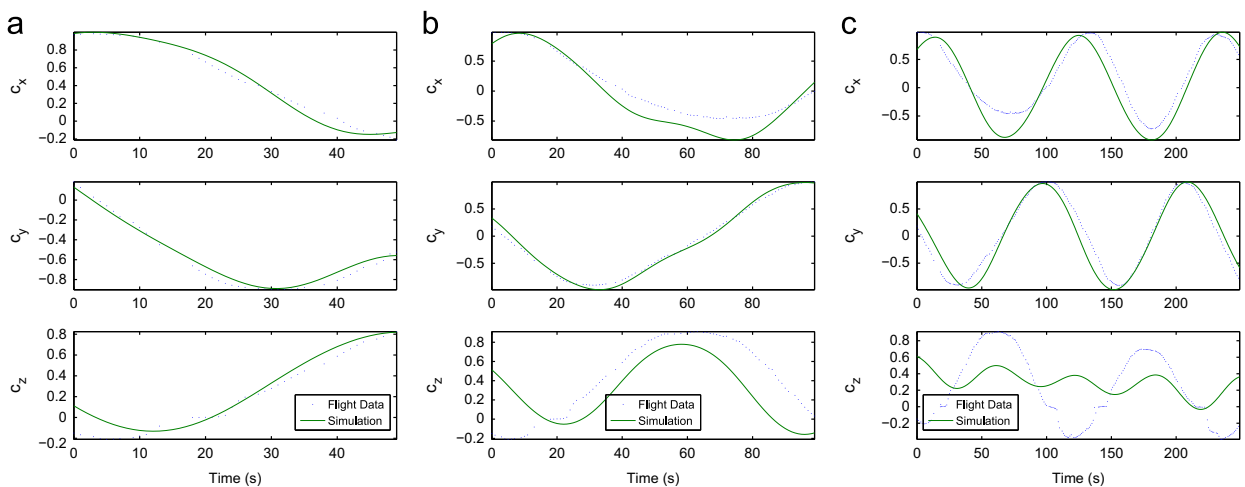


**Fig. 8.** Optimization of initial condition only over windows of (a) 50 s, (b) 100 s and (c) 250 s.

Initial attempts to run the optimization with both the initial state and parameters as free variables led to divergence, likely due to having too many free parameters. Instead the optimization was initially run with the parameters held constant and only the initial state,  $x_0$ , free. The simulation was run over windows of 50 s, 100 s and then 250 s, as illustrated in Fig. 8.

Once a good fit for the initial state is found, then the parameters of the dynamics model could be unfrozen and included in the optimization. Fitting only the initial condition at first takes advantage of the low torque environment, as over the short windows, the motion is close to torque free. The optimization algorithm can focus on just the kinematic state and does not over fit the dynamics parameters and attain unphysical values.



## 2.8. Data sources

The work in this paper utilized flight data from two different nano satellites, O/OREOS and RAX-1, described in this section. Neither nano satellites included any deployable or flexible structures, so changes in the moments of inertia after launch are unlikely. The errors in the attitude dynamics model are expected to mostly arise from the uncertainty in the permanent dipole.

The Organism/Organic Exposure to Orbital Stresses (O/OREOS) spacecraft is a 3U nano satellite that launched in November 2010 from Kodiak, AK into an approximately 650 km altitude,  $72^\circ$  low Earth orbit. O/OREOS, illustrated in Fig. 9, carried two astrobiology payloads to study the survivability and viability of the space environment to live organisms and organics respectively. The passive attitude stabilization system consisted of permanent dipoles aligned along the long (z) axis, and hysteresis rods in the plane perpendicular to the long axis. O/OREOS had no dedicated onboard attitude sensors, however the spacecraft bus did monitor solar panel currents. Panels were only mounted on the  $\pm x$  and  $\pm y$  faces, so only an estimate of the x and y components of the solar vector was available. The spacecraft employed a fixed voltage set point for the solar arrays.

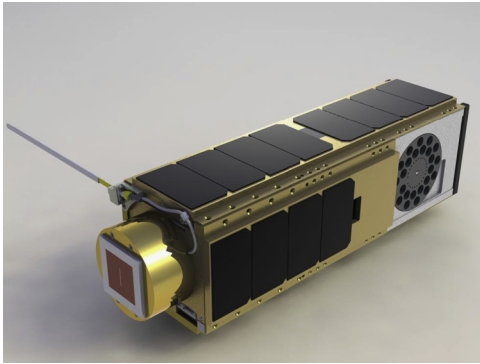


Fig. 9. NASA Ames Research Center's O/OREOS 3U CubeSat.

Included on the same launch manifest as O/OREOS was the first Radio Aurora Explorer satellite, RAX-1, a 3U CubeSat that was developed to study magnetic field-aligned plasma irregularities in Earth's ionosphere [10], and is illustrated in Fig. 1. The satellite was developed jointly by SRI International and the University of Michigan, and the science payload is an ultra high frequency (UHF) radar receiver. Working in conjunction with ground based incoherent scatter radar stations, the purpose of the mission was to improve the understanding of the ionospheric irregularities with the ultimate goal of enabling short-term forecasting. The passive magnetic attitude control system consists of four permanent magnets aligned with the long z axis and two strips of HyMu80 soft magnetic material mounted in two axes perpendicular to the permanent magnets. RAX-1 included a full suite of attitude sensors consisting of multiple photodiodes, two three-axis magnetometers, and a three-axis rate gyroscope [11]. To improve the accuracy of the magnetometer and photodiode measurements attitude independent calibration was performed, with an on-orbit magnetometer calibration algorithm developed to mitigate the effect of nearby electronics on the magnetometers, which are embedded in the spacecraft [12]. The calibrated photodiode readings were used to create a reliable estimate of the sun vector in the body frame. In the work described in this paper the calibrated magnetometer and gyro data were used solely for independent verification of the solution.

Both O/OREOS and RAX-1 recorded data at 1 Hz. TLE ephemerides were available for both spacecrafts with updates occurring about every 24 h, leading to maximum orbit propagation errors of a few kilometers. Orbit propagation was performed from the TLEs using a reference implementation of the SGP4 [13] algorithm.

## 3. Results

The optimization algorithm was run on data from the O/OREOS and RAX-1 spacecraft. The MATLAB function `fmincon` with the 'active-set' algorithm was used to perform the optimization.

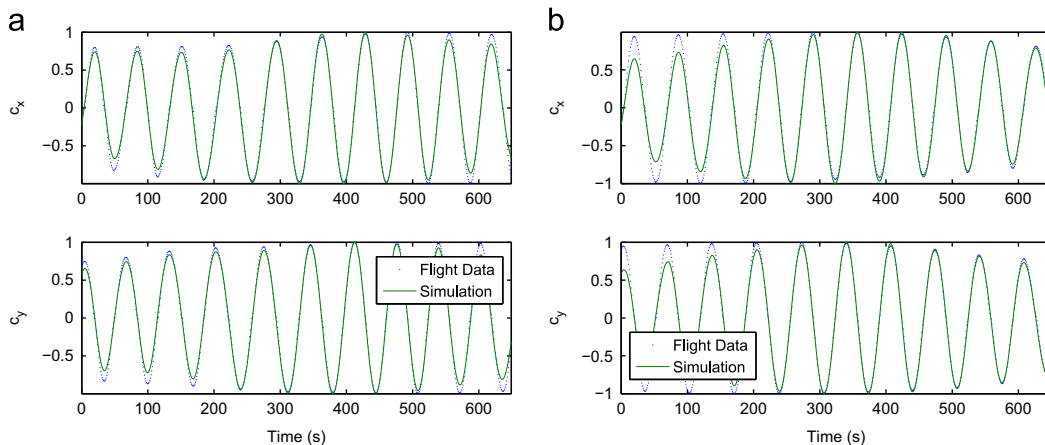


Fig. 10. Comparison of solar vector components for O/OREOS. (a) 11-Apr-2011. (b) 04-Apr-2011.

3.1. O/OREOS

In Fig. 10(a) the measured solar vector as estimated from solar panel currents is plotted alongside the simulated solar vector, as determined from the solution of the optimization.

Using laboratory measurements of similar hardware, the total z-aligned dipole for O/OREOS was estimated to be  $15.5 \text{ A m}^2$ . The optimized value for the permanent dipole was  $[0.31 \text{ } -0.02 \text{ } 16.9]^T \text{ A m}^2$ , which is not dissimilar from the assumed installed value. The solved permanent dipole is close to z-aligned and has a reasonable order of magnitude.

To demonstrate the problems with using the incorrect dipole, the optimization was run again on the same data set, but forcing the modeled permanent dipole strength,  $M_p$ , to the pre-launch measured value. The minimal value of the cost function obtained was over four times larger than that found by calibrating the dipole.

An attempt to verify the solved permanent dipole can be made by performing the optimization on a different data set. Fig. 10(b) shows the result of a second optimization run on a different data set. In this second case the optimal permanent dipole was found to be  $[0.35 \text{ } 0.02 \text{ } 19.8]^T \text{ A m}^2$ , which is similar but not the same. It is possible

that the parameters were over-fitted to the data which is made more likely due to the short available data run and having only  $x$  and  $y$  components available.

To test for over-fitting, a final optimization was performed that found two sets of initial conditions and a single permanent dipole that best explained both sets of data. This jointly optimized permanent dipole was found to be  $[0.30 \text{ } 0.00 \text{ } 17.4]^T \text{ A m}^2$ . The cost functions associated with each optimization are given in Table 2. The jointly optimized dipole is still a close fit, with little cost difference to the individually optimized dipoles.

While the results from the optimization on O/OREOS look promising, little hard conclusions can be drawn about the success of the algorithm due to the scarcity of the data and the limited sensor suite available. By contrast RAX-1 offered richer data sets both in terms of having longer time periods of data collection, and of having more sensors that can be used for verification.

3.2. RAX-1

The optimization was run for data from RAX-1, with a sample set of results shown in Fig. 11. For clarity in the figure, only the first 1500 s of the data run are shown.

Before launch the permanent dipole was assumed to be z-aligned with a strength of  $3.2 \text{ A m}^2$ . The estimation

Table 2

Cost functions for optimization of the permanent dipole and initial attitude for two data sets for the O/OREOS spacecraft.

Dipole optimization used	04-Apr-2011	11-Apr-2011
None (pre-launch)	0.1178	0.3764
Individual	0.1036	0.0812
Joint	0.1047	0.0819

Table 3

Cost functions for optimization of the permanent dipole and initial attitude for two data sets for the RAX-1 spacecraft.

Dipole optimization used	15-Dec-2010	30-Dec-2010
None (pre-launch)	0.9976	0.9090
Individual	0.1619	0.1636

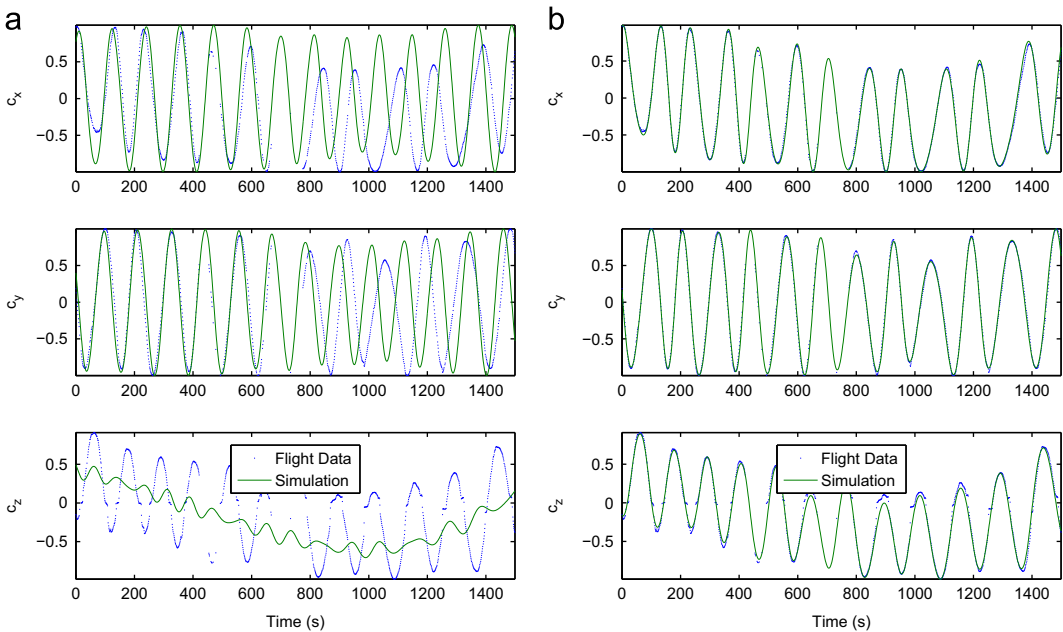


Fig. 11. Comparison of solar vector components for RAX-1 – 30-Dec-2010. (a) Prior to Calibration. (b) With Calibrated Permanent Dipole and Inertia Matrix.

algorithm returned an optimal dipole of  $[0.14 \ 0.02 \ 1.09]^T \text{ A m}^2$ , markedly different from the pre-launch value both in magnitude and alignment. Fig. 11 also includes the best fit over the same dataset if the pre-launch dipole was used in the dynamics model, and shows how much the observed and simulated data differ. The cost functions associated with each optimization are listed in Table 3. The pre-launch estimated and calibrated inertia matrices are shown in Eq. (53), and as suspected are similar.

$$I_{\text{pre}} = \begin{bmatrix} 0.018 & 0 & 0 \\ 0 & 0.018 & 0 \\ 0 & 0 & 0.006 \end{bmatrix},$$

$$I_{\text{opt}} = \begin{bmatrix} 0.0185 & 0.0000 & 0.0001 \\ 0.0000 & 0.0183 & 0.0004 \\ 0.0001 & 0.0004 & 0.0043 \end{bmatrix} \quad (53)$$

The RAX-1 spacecraft also includes magnetometers and gyros, and as the data from these sensors were not used in the estimation, they can be used to verify the simulated attitude profile. Fig. 12(a) compares the calibrated magnetometer readings to those generated by the simulation and Fig. 12(b) compares the onboard gyro data to the angular rates from the simulation. On the average the magnetometer readings agree within  $0.4 \text{ A m}^{-1}$ . The observed offset between the simulated angular velocity and the gyro readings is due to the bias in the gyro.

As was done for the data from O/OREOS, an optimization was also performed on different data sets from RAX-1. Fig. 13 compares simulated and measured solar vector data for data sets from 15 and 30 days earlier. The optimized dipoles from the two data sets were within 2% of the optimal dipole found from the first RAX-1 dataset studied: for 01-Dec-2010, the optimal dipole was found to be  $[0.15 \ 0.01 \ 1.09]^T \text{ A m}^2$ ; and for 15-Dec-2010,  $[0.15 \ 0.02 \ 1.09]^T \text{ A m}^2$ .

The closeness of the two optimal dipoles and the cross check against independent bus data builds a strong case for the validity of the dynamics model and solved parameters. The data from 01-Dec-2010 is only 10 days after launch, and as can be seen by the higher frequency of the oscillations in Fig. 13(a), the spacecraft is still de-tumbling. However the estimation algorithm still performs very well, and still returns a similar optimized dipole. This provides further validation that the assumed form of the dynamics model is correct.

### 3.3. Attitude determination

The optimization described in Section 2 necessarily propagates a kinematic attitude state, hence providing a batch estimate of attitude in addition to calibrating the parameters of the dynamics model. As with the calibration, this batch attitude estimate is dependent on only solar vector observations. While truth attitude data were not available, two metrics were used to estimate the performance of the batch method. Firstly, an independent estimate of the attitude of RAX-1 was made using all the available satellite attitude sensors. Secondly, an estimate of the uncertainty of the batch attitude solution was made using a Monte Carlo analysis.

The independent estimate of RAX-1's attitude was made using a recursive filter that used all the available flight data, which included two magnetometers and a MEMS gyro in addition to the photodiodes. This recursive filter, referred to in this paper as the full filter, is based upon the multiplicative extended Kalman filter [14] and in simulation is shown to have an expected  $1 \sigma$  pointing error of  $1.4^\circ$ . A complete description of the full filter can be found in Ref. [6].

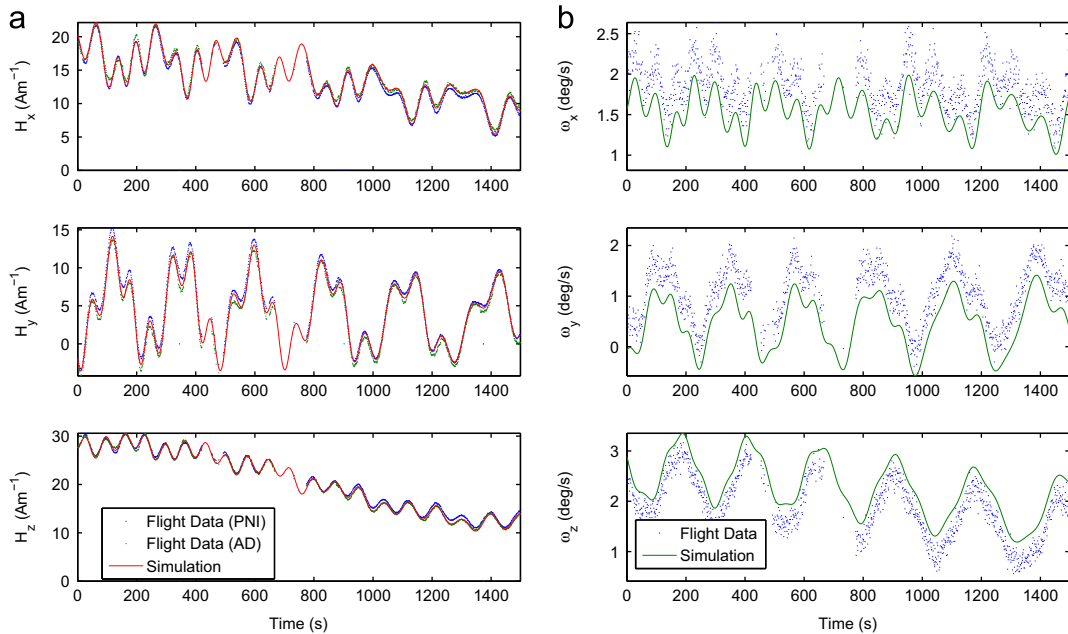
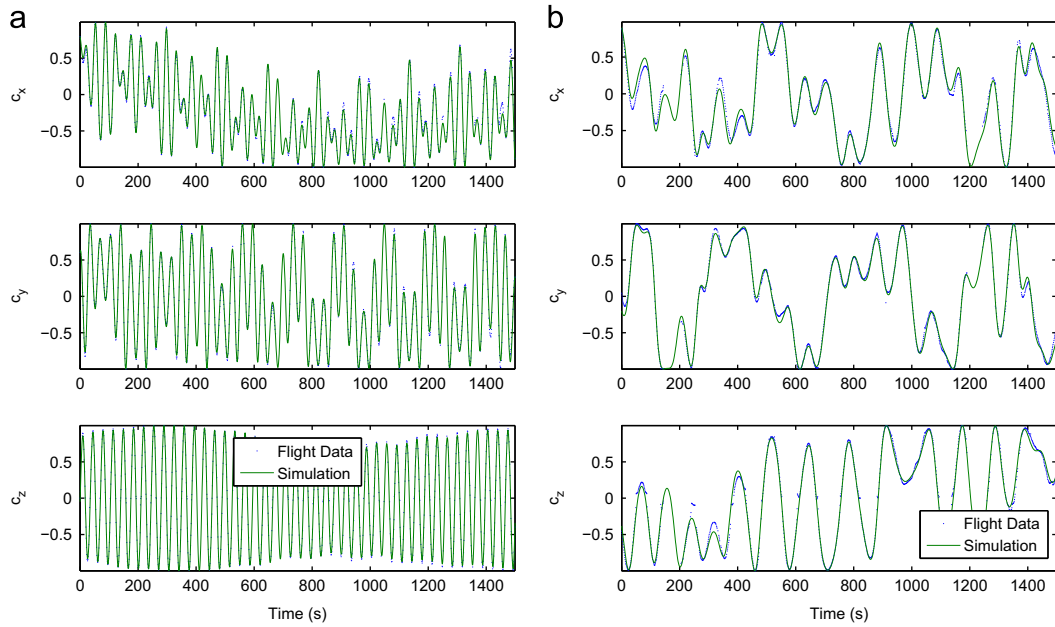
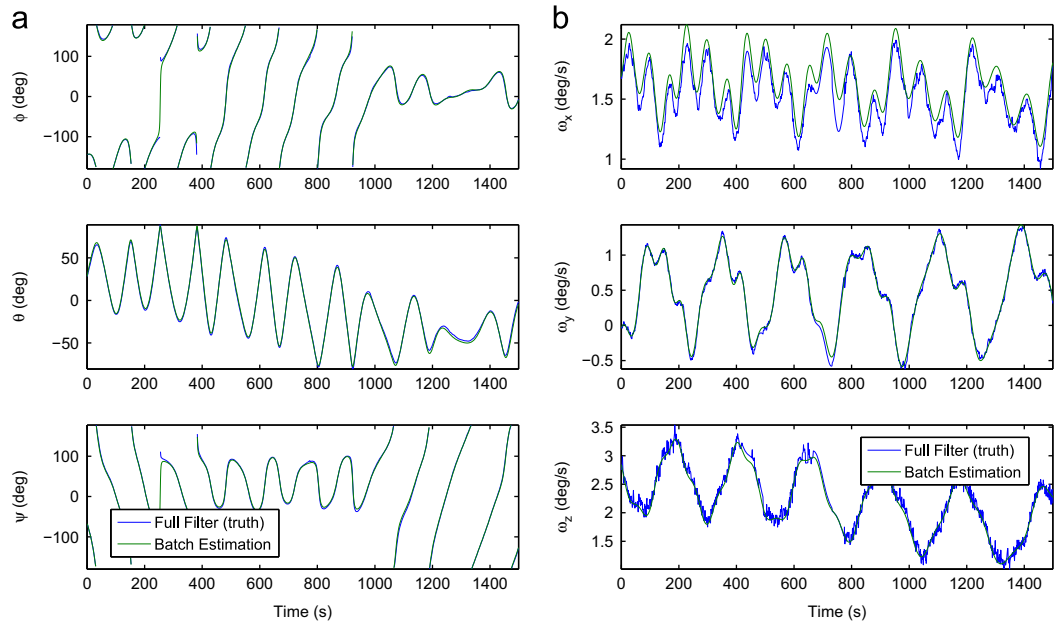


Fig. 12. Comparison of simulated data to alternative bus data sources. RAX-1. 30-Dec-2010. (a) Magnetometer. (b) IMU gyro.



**Fig. 13.** Comparison of bus data and simulated data – solar vector components for RAX-1. (a) 01-Dec-2010. (b) 15-Dec-2010.



**Fig. 14.** Attitude profiles from calibration compared to independent attitude estimate. (a) Attitude estimate. (b) Angular rate estimate.

The attitude and attitude rate profiles as generated by the batch calibration are plotted in Fig. 14, along with the attitude estimate of the full filter. Fig. 15 plots the error in the attitude and attitude rates, defined as the difference between the batch estimate and the full filter. Finally Fig. 16 plots the total attitude error of the batch estimate. Nominal attitude errors in each axis are between  $1.25^\circ$  and  $3.25^\circ$ , with a total attitude error of  $4.5^\circ$ , as listed in Table 4. Attitude rate errors are nominally  $0.1^\circ\text{s}^{-1}$  in each axis.

The uncertainty in the batch attitude solution was estimated using Monte Carlo simulation. The batch optimization

described previously was run multiple times over the same data set, but each time random noise was added to the measured solar vector. The added noise was chosen to match the observed noise in the photodiodes, and was equivalent to a  $1\sigma$  angular error of  $2.3^\circ$  in the direction of the solar vector. The difference between the attitude profile determined in each Monte Carlo trial and the attitude profile of the nominal solution was computed, and the standard deviations of these differences are listed in Table 4. The estimated uncertainties generated from Monte Carlo simulation match the previously computed attitude errors well, although appear to slightly

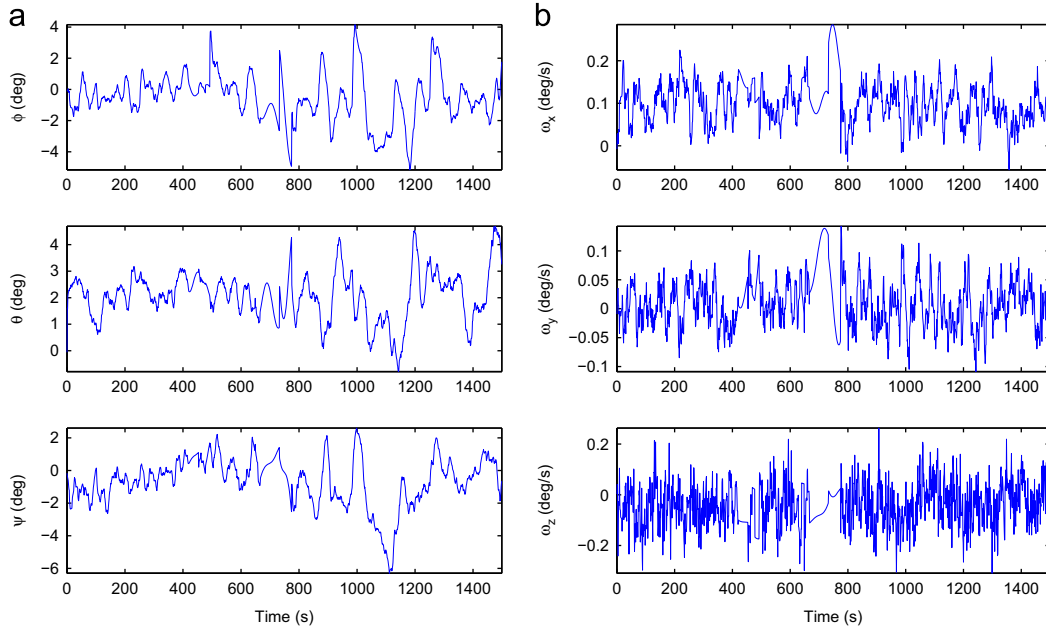


**Fig. 15.** Difference between the attitude profile from calibration and the independent attitude estimate. (a) Attitude errors. (b) Angular rate errors.

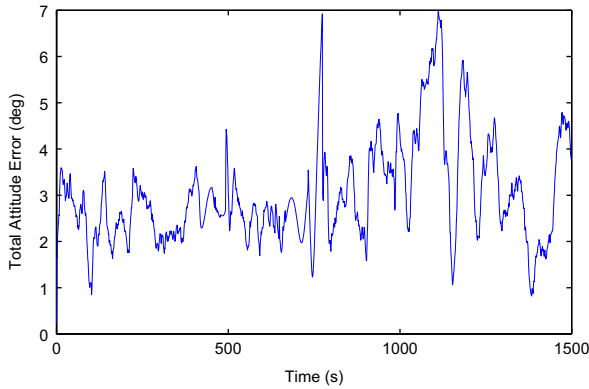


**Fig. 16.** Total pointing difference between calibration and independent attitude estimate.

**Table 4**  
Batch attitude  $1\sigma$  errors and uncertainties for RAX-1.

Euler angle	Full filter error (deg)	Monte Carlo uncertainty (deg)
$\phi$	2.53	1.51
$\theta$	1.28	0.52
$\psi$	3.39	1.95
Total	4.55	3.66

underestimate them. However, the truth metric used to compute those attitude errors, the full filter, itself has a known uncertainty of  $1.4^\circ$  in total attitude.

#### 4. Conclusion

A batch estimation algorithm was developed that is able to calibrate the unknown parameters of the attitude dynamics model on orbit, and provide an estimate of the

attitude of a passively magnetically stabilized nano satellite. The estimation takes the form of a non-convex optimization. The algorithm was tested against actual flight data from two nano satellites, and the resultant parameters found through optimization remained physically realizable. The importance of performing this on orbit calibration of magnetic properties was shown as even in steady state, when only a permanent dipole was assumed, the permanent dipole that best explained the observed data differed from pre-launch measurements.

#### Acknowledgments

The research described in this paper was funded by a Grant from the National Aeronautics and Space Administration. Flight data from NASA Ames Research Center's O/OREOS nano satellite was provided by Santa Clara University. Flight data from the RAX-1 nano satellite was provided by the University of Michigan. The RAX-1 mission was funded by the U.S. National Science Foundation.

#### Appendix A. Notation

Symbol	Description	Units
$\mu_0$	permeability of free space $= 4\pi \times 10^{-7}$	$\text{H m}^{-1}$
$\omega$	angular rate, body frame	$\text{rad s}^{-1}$
$q$	unit quaternion, inertial to body frame	
$n_i$	unit vector along $i$ th permeable rod	
$c$	solar unit vector, body frame	
$c_{\text{ECI}}$	solar unit vector, inertial frame	
$B$	induced magnetic flux density in a permeable material	T
$B_r$	remanence flux density of permeable material	T
$B_s$	saturation flux density of permeable material	T



$H$	external magnetic field, body frame	$A\ m^{-1}$
$H_{ECI}$	Earth's magnetic field, ECI frame	$A\ m^{-1}$
$H_c$	coercivity of permeable material	$A\ m^{-1}$
$M$	total dipole of magnetic material	$A\ m^{-2}$
$M_P$	permanent dipole in a permanent magnet	$A\ m^{-2}$
$S$	modified induced magnetic flux density in a permeable material	
$V$	volume of permeable material	$m^3$
$I$	moment of inertia, body frame	$kg\ m^2$
$T$	external torque, body frame	$N\ m$

## References

- [1] T.W. Flatley, D.A. Henretty, A magnetic hysteresis model, in: K.R. Hartman (Ed.), *Flight Mechanics/Estimation Theory Symposium* 1995, 1995, pp. 405–415.
- [2] T. Bleier, P. Clarke, J. Cutler, L. DeMartini, C. Dunson, S. Flagg, A. Lorenz, E. Tapio, Quakesat Lessons Learned: Notes from the Development of a Triple Cubesat. URL ([http://www.quakefinder.com/research/quakesat-ssite/documents/Lessons\\_Learned\\_Final.pdf](http://www.quakefinder.com/research/quakesat-ssite/documents/Lessons_Learned_Final.pdf)).
- [3] J. Crassidis, F. Markley, Y. Cheng, Survey of nonlinear attitude estimation methods, *J. Guid. Control Dynam.* 30 (1) (2007) 12.
- [4] R. Burton, J. Starek, S.M. Rock, A new method for simulating the attitude dynamics of passively magnetically stabilized spacecraft, in: *Proceedings of the 22nd AAS/AIAA Space Flight Mechanics Meeting, AAS/AIAA, AAS/AIAA, Charleston SC, 2012*. URL: ([http://www.stanford.edu/group/arl/cgi-bin/drupal/sites/default/files/public/publications/burton\\_aas\\_12\\_169.pdf](http://www.stanford.edu/group/arl/cgi-bin/drupal/sites/default/files/public/publications/burton_aas_12_169.pdf)).
- [5] International Association of Geomagnetism and Aeronomy, Working Group V-MOD. Participating members, C.C. Finlay, S. Maus, C.D. Beggan, T.N. Bondar, A. Chambodut, T.A. Chernova, A. Chulliat, V.P. Golovkov, B. Hamilton, M. Hamoudi, R. Holme, G. Hulot, W. Kuang, B. Langlais, V. Lesur, F.J. Lowes, H. Lühr, S. Macmillan, M. Manda, S. McLean, C. Manoj, M. Menvielle, I. Michaelis, N. Olsen, J. Rauberg, M. Rother, T. J. Sabaka, A. Tangborn, L. Tøffner-Clausen, E. Thébault, A.W.P. Thomson, I. Wardinski, Z. Wei, T.I. Zvereva, *International geomagnetic reference field: the eleventh generation, Geophysical Journal International* 183 (3) (2010) 1216–1230. <http://dx.doi.org/10.1111/j.1365-246X.2010.04804.x>.
- [6] R. Burton, Attitude Determination of Passively Magnetically Stabilized Nano Satellites, Ph.D. Thesis, May 2013. URL: (<http://purl.stanford.edu/hf898cp8579>).
- [7] F. Santoni, M. Zelli, Passive magnetic attitude stabilization of the unisat-4 microsatellite, *Acta Astronaut.* 65 (5–6) (2009) 792–803, <http://dx.doi.org/10.1016/j.actaastro.2009.03.012>. URL (<http://www.sciencedirect.com/science/article/pii/S0094576509001568>).
- [8] G. Wahba, et al., A least squares estimate of satellite attitude, *SIAM Rev.* 7 (3) (1965) 409.
- [9] F. Markley, Attitude determination using vector observations and the singular value decomposition, *J. Astronaut. Sci.* 36 (3) (1988) 245–258.
- [10] J. Cutler, J. Springmann, S. Spangelo, H. Bahcivan, Initial flight assessment of the radio aurora explorer, in: *Proceedings of the 25th Annual AIAA/USU Conference on Small Satellites*, Logan, Utah, August 2011.
- [11] J. Springmann, A. Sloboda, A. Klesh, M. Bennett, J. Cutler, The attitude determination system of the rax satellite, *Acta Astronaut.* 75 (2012) 120–135.
- [12] J. Springmann, Attitude-independent magnetometer calibration with time-varying bias, in: *Proceedings of the 25th Annual AIAA/USU Conference on Small Satellites*, Logan, Utah, August 2011.
- [13] D. Vallado, P. Crawford, R. Hujsak, T. Kelso, Revisiting spacetrack report# 3, *AIAA J.* 6753 (2006) 2006.
- [14] E. Lefferts, F. Markley, M. Shuster, Kalman filtering for spacecraft attitude estimation, *J. Guid. Contr. Dynam.* 5 (5) (1982) 417–429.